ADVANCED ENERGY MATERIALS
www.advenergymat.de

Kinetically-Enhanced Gradient Modulator Layer Enables Wide-Temperature Ultralong-Life All-Solid-State Lithium-Sulfur Batteries

Hao Li, Lianmeng Cui, Fanglin Wu, Jian Wang, Yapeng Cheng, Canhuang Li, Jiangping Song, Yafeng Li, Dan Liu, Andreu Cabot,* Chaoqi Zhang, and Haolin Tang**

Inadequate ionic transport across the electrode/electrolyte interface hampers the lithium-sulfur reaction kinetics, thereby limiting the electrochemical performance of all-solid-state lithium-sulfur batteries (ASSLSBs). Herein, a kinetically-enhanced gradient modulator layer (KEGML) is proposed and fabricated via potential modulation. In situ/ex situ analyses reveal the optimal modulated potential difference driving the chemical reaction between Li ions and the P_2S_5 pre-interphase product for stabilized KEGML and maintained full-sulfur conversion. Cryo-focused ion beam-scanning electron microscopy characterization and *ab-initio* molecular dynamics confirm the interfacial reinforcement by gradient uniformization of ion transport and enhanced interface stability by efficiently avoiding the side effects between sulfur/sulfides solid electrolyte/carbon, respectively. As a result, an eightfold increase in ionic transport capability is achieved with KEGML at the end of the 200 cycles. Impressively, KEGML-based ASSLSBs not only accelerate the redox conversions but also display an exceptional cycling stability of a specific capacity of 1578.9 mAh g^{-1} for ≈1.5 years with a 99.9% capacity retention and a high areal capacity of 13 mAh cm^{-2} over 200 cycles, which is among the record-level. Even in the ambient environment from 60 °C to as low as −30 °C, it exhibits excellent adaptivity attributed to the fast kinetics, shedding light on future practical applications.

1. Introduction

All-solid-state lithium-sulfur battery (ASSLSB) technologies have been explored not only to significantly enhance safety by eliminating the flammable liquid component but also to address the issue of lithium polysulfide dissolution.[1–7] This exploration potentially unlocks ASSLSBs as a key future energy storage technology, with a high theoretical specific capacity of 1675 mAh g^{-1}.[4,5] Recently, sulfide solid-state electrolytes (SSEs) have been extensively investigated due to their remarkable room-temperature ionic conductivity (10^{-2} S cm^{-1}), moderate Young's module (10–20 GPa), and excellent compatibility with sulfide compounds.[8,9] Nevertheless, the slow electronic and ionic transport mainly attributed to the poor wettability of all-solid-state particles at the three-component interface formed among active sulfur, ion-conducting sulfide SSEs, and carbon electronic

H. Li, L. Cui, F. Wu, Y. Li, H. Tang
State Key Laboratory of Advanced Technology for Materials Synthesis and Processing
Wuhan University of Technology
Wuhan, Hubei 430070, P. R. China
E-mail: thln@whut.edu.cn

H. Li, F. Wu, Y. Li, D. Liu, H. Tang
Hubei Key Laboratory of Fuel Cells
Wuhan University of Technology
Wuhan, Hubei 430070, P. R. China
E-mail: danielliu@whut.edu.cn

The ORCID identification number(s) for the author(s) of this article can be found under https://doi.org/10.1002/aenm.202501259

DOI: 10.1002/aenm.202501259

J. Wang
Karlsruhe Institute of Technology (KIT)
P.O. Box 3640, D-7621 Karlsruhe, Germany

J. Wang
Helmholtz Institute Ulm (HIU)
Helmholtzstrasse 11, D-89081 Ulm, Germany

Y. Cheng, C. Li, A. Cabot
Catalonia Institute for Energy Research – IREC Sant Adrià de Besòs
Barcelona 08930, Spain
E-mail: acabot@irec.cat

J. Song, H. Tang
Foshan Xianhu Laboratory of the Advanced Energy Science and Technology
Guangdong Laboratory
Foshan 528200, P. R. China

A. Cabot
ICREA Pg. Lluis Companys
Barcelona 08010, Catalonia, Spain

C. Zhang
College of Materials Science and Engineering
Fuzhou University
Fuzhou, Fujian 350108, P. R. China

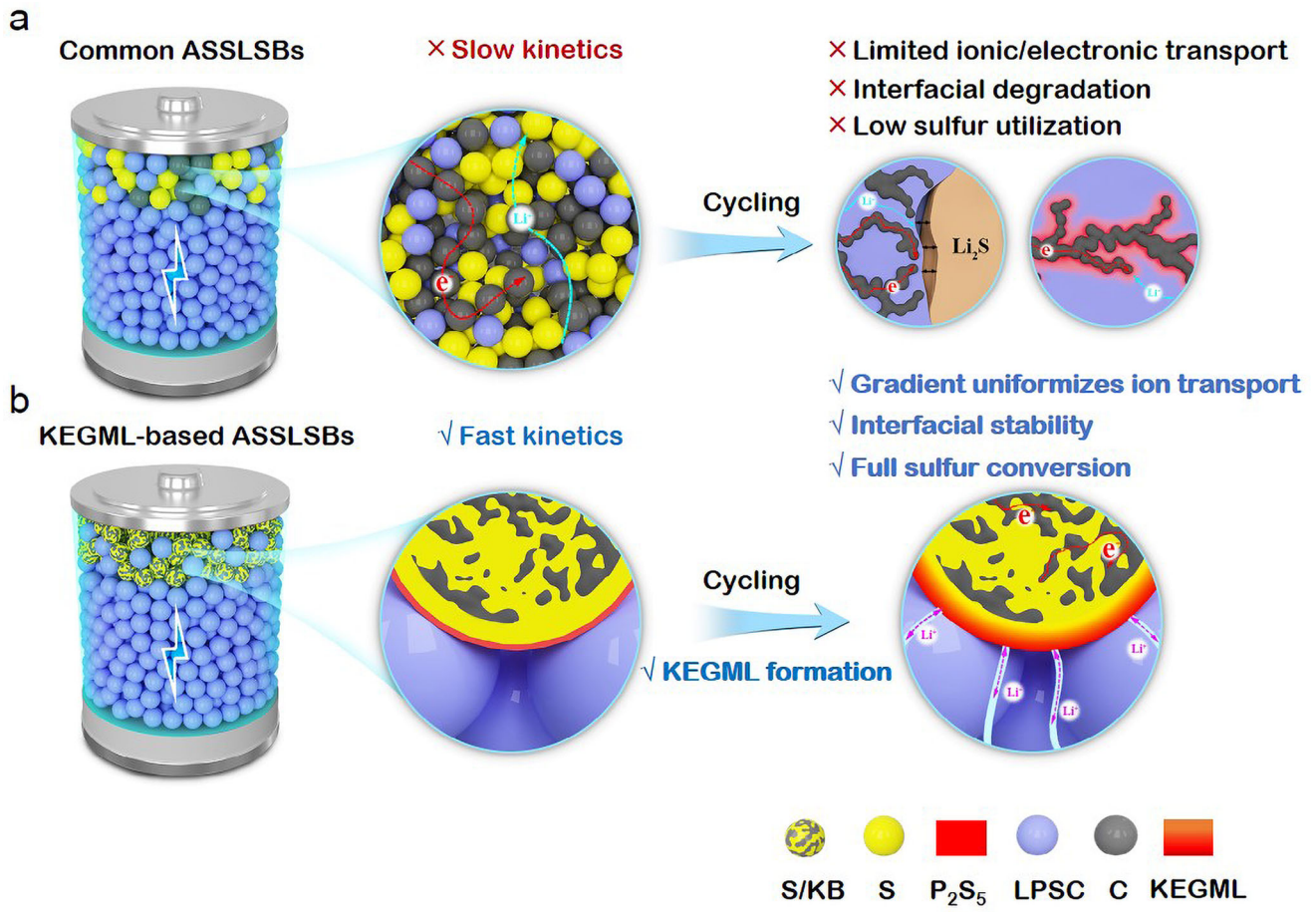

Figure 1. Schematic illustrations of a) common ASSLSBs and b) KEGML-based ASSLSBs.

conductor greatly limits the utilization of sulfur as depicted in **Figure 1a**, resulting in low Coulombic efficiency (CE) and capacity degradation over long-term cycling.[10,11] Although there is currently limited research on the interface between sulfur/sulfides and sulfide SSEs, theoretical calculations predict that the possibility of interfacial mutual consumption may result in slow reaction kinetics and poor cycling stability.[12,13]

Efforts have been made to enhance ionic/electronic transport at the three-component interface,[14–25] but they rarely simultaneously consider the interfacial decomposition issue caused by side reactions and inevitable contact with sulfide SSEs.[26,27] Moreover, studies are increasingly using transition metal sulfides as sulfur hosts and active materials, introducing catalysts, and employing solid solutions (e.g., Li_2S-LiI and Li_2S-Li_2O-LiI).[28–37] These methods aim to reduce the contact area between carbon and sulfide SSE interfaces and enhance ion transport around sulfur.[28–37] Nevertheless, the results of this research still have limitations in terms of theoretical capacity (<1200 mAh g^{-1}) or cycle life.[28,29,31–37] Additionally, the potential instability of sulfide SSEs under their widely applied potential windows remains insufficiently investigated. Due to the slow reaction kinetics of solid-state chemical reactions, ASSLSBs require a wider potential range compared to liquid-state Li-S batteries for full-sulfur conversion.[38] However, the electrochemical stability range of sulfide SSEs is relatively narrow.[12,38,39] The degradation products, such as P_2S_5, Li_3P, and Li_2S, increase the discharge product complexity,[40] hindering electron/ion transport and further deteriorating battery performance.[38] Janek et al.'s research suggests that effective ion transport can occur within a wider potential range to enhance the achievable capacity of ASSLSBs without compromising overall ionic transport.[38] In other words, the possibility of providing a greater potential drive to achieve complete sulfur conversion without significantly affecting lithium-ion transport.

To date, there is no consensus on the applied potential range for the sulfide SSE-based ASSLSBs. Various potential ranges have been reported, such as 0.8–2.4 and 1.5–3.0 V versus Li^+/Li, 0.7–2.7 and 0.5–3.0 V versus Li^+/Li-In in ASSLSBs using S/C composite cathode and LPSC as SSEs.[16,18,41,42] Matter-of-factly, these researchers have not provided detailed explanations for their choice or the potential impact of the possible decomposition of LPSC within this specific range. Originally, Janek et al. reported that a higher charge cut-off potential results in a higher reversible redox capacity but hinders ion transport and increases the cathode overpotential (oxidative degradation).[38,39] The lower discharge cut-off potential has been found to gradually lead to an unstable three-component interface, increased interfacial impedance, and deteriorated battery cycling performance

(reductive degradation).[38,39] They further investigated the long-term stabilities with varying cycling potential ranges and found that increasing the discharge cut-off potential limits sulfur conversion but improves cycling performance and long-term durability.[39] Except for Kim et. al.'s report,[30] there is still limited research on the complex correlations between applied potential ranges, resulting in interphase and discharge products, and their electrochemical performance. However, this 1500-cycle stability was achieved at the expense of limited solid-solid conversion from S to Li_2S to promote a Li_2S_2-dominant discharge product.[30] The sluggish reaction of Li_2S to S is considered to be the bottleneck for long-term cycling.[38] Therefore, modulating and utilizing appropriate discharge cut-off potential for enabling fast reaction kinetics and forming a stable interphase is crucial for sulfur cathodes as it directly affects complete sulfur conversion and ensures a prolonged lifespan.

Herein, the applied potential modulation has been investigated to control the kinetically enhanced gradient modulator layer (KEGML) (Figure 1b). The KEGML is applied to the surface of carbon/sulfur particles to enhance the interfacial performance of the sulfur cathode. It can inhibit LPSC decomposition and improve interfacial stability by blocking direct contact between carbon and LPSC. Furthermore, it not only serves as an ion-conducting layer to facilitate the Li^+ ion transport but also acts as a gradient modulator layer to enhance interface contact. In detail, an interfacial pre-reaction occurs between a small amount of phosphorus (P) and S to form a P_2S_5 on the S/KB composite (S/KB@P), followed by modulation of the initial discharge cut-off potential to facilitate the reaction between the P_2S_5 pre-interphase and Li^+ ions, gradually forming KEGML in ASSLSBs. Different applied potential ranges result in varying concentrations of Li^+ ions reacting with the P_2S_5 pre-interphase, leading to different chemical states of the KEGML. The structural and chemical properties of the KEGML during the dynamic potential modulating were investigated by cryo-focused ion beam-scanning electron microscopy (Cryo-FIB-SEM), and in situ Raman analysis. Combining with ionic transport capability during 200-cycling, distribution of Relaxation Times (DRT) analyses of the interfacial impedance evolution, and ab-into molecular dynamics (AIMD), KEGML-based ASSLSBs show great potential in improving Li^+ ion transport and stabilizing the three-component interface, leading to simultaneous complete-sulfur solid-state chemical conversion as well as ultra-long cycle stability.

2. Results and Discussion

2.1. Characterization and Formation of KEGML

The S content within the S/KB composite is 65% (Figure S1, Supporting Information). Loading with S leads to a significant decrease in specific surface area and eliminates any notable peaks in pore size distribution, indicating deposition of sulfur both on the outer surface and within the pores of KB particles (Figure S2, Supporting Information).[43] There is no apparent change in the morphology of the S/KB@P composite before and after compounding P (Figure S3, Supporting Information). TEM images reveal irregular spherical morphologies with a single-particle diameter of 50–100 nm (Figure S4, Supporting Information). Figures S5 and S6 (Supporting Information) reveal a homogeneous distribution of S and P elements. There are no peaks corresponding to crystalline S that are observed, which is a common phenomenon using vapor deposition (Figure S7a, Supporting Information).[43,44] Additionally, the absence of peaks associated with P in the S/KB@P aligns with its amorphous nature and low content. After comparing the XPS spectra of the S/KB@P composite (Figure S7b,c, Supporting Information) with that of commercial P_2S_5 (Figure S8 and Table S1, Supporting Information), it is found that the pre-reactant product between S and P on the surface of S/KB particles is P_2S_5. The characteristic peaks of P_2S_5 can also be detected in Raman spectra, confirming the formation of P_2S_5 after the pre-reaction between S and P during long-time ball-milling (Figure S9a, Supporting Information). Furthermore, the thickness of the P_2S_5 layer is ≈8 nm in the S/KB@P composite, which is evidenced by conducting In-depth XPS analyses (Figure S9b, Supporting Information).

Under a generally operated potential range of 0.5–2.5 V versus Li^+/Li-In,[25,43,45–48] the initial discharge capacity of the S/KB cathode is 1489 mAh g^{-1} and decreased to 656 mAh g^{-1} after 100 cycles (Figure S10, Supporting Information). To clarify the chemical state of the electrode, peaks related to S and Li_xS are observed in the S 2p spectra after 10 cycles (Figure S11 and Table S2, Supporting Information).[39] Figure S12 (Supporting Information) shows the S 2p XPS spectra of commercial Li_2S, solid-state electrolyte Li_6PS_5Cl (LPSC), and the LPSC sample after cycling as references. The poor electrochemical performance can be attributed to slow reaction kinetics, leading to incomplete conversion of S and partial LPSC decomposition.[38–40] In this regard, the unique potential-modulated KEGML can effectively solve the aforementioned problems. Through an extension of the initial discharge cut-off potential, the pre-interphase P_2S_5 at S/KB undergoes a reaction with Li^+ ion, resulting in the formation of KEGML. The initial electrochemical window of the ASSLSB is extended by the electrochemical window provided by the KEGML (**Figure 2a**). A conventional electrochemical window (0.5–2.5 V vs Li^+/Li-In) is adopted in the subsequent cycle to ensure the existence of KEGML. The effective electrochemical window of KEGML is its expanded electrochemical window that subtracts the conventional electrochemical window ($\Delta\varphi$ (KEGML)), which determines the ion concentration involved in interfacial reactions and the chemical state of KEGML. The impact of different chemical states of KEGML on battery performance is further investigated by regulating $\Delta\varphi$ (KEGML). The electrochemical performance of the S/KB@P cathode is optimized at an initial discharge cut-off potential of 0 V vs Li^+/Li-In (Figure 2b,c), achieving stable cycling at a specific capacity of 1579 mAh g^{-1} within the subsequent potential window of 0.5–2.5 V versus Li^+/Li-In. However, when initially discharged to −0.5 V versus Li^+/Li-In, stable cycling is observed but with a decrease in discharge capacity.

Hayashi et al.[34] demonstrated that investigating the reaction mechanism of Li_2S/S in a Li_2S-LiI-C cathode is possible by using highly crystalline LiI as an ionic conductor for XPS analysis to avoid the interference of the same chemical composition (S and LPSC). Following this approach, S/KB@P-LiI cathodes were prepared without LPSC for a more detailed analysis. Cyclic voltammetry (CV) experiments in the initial cycle were first

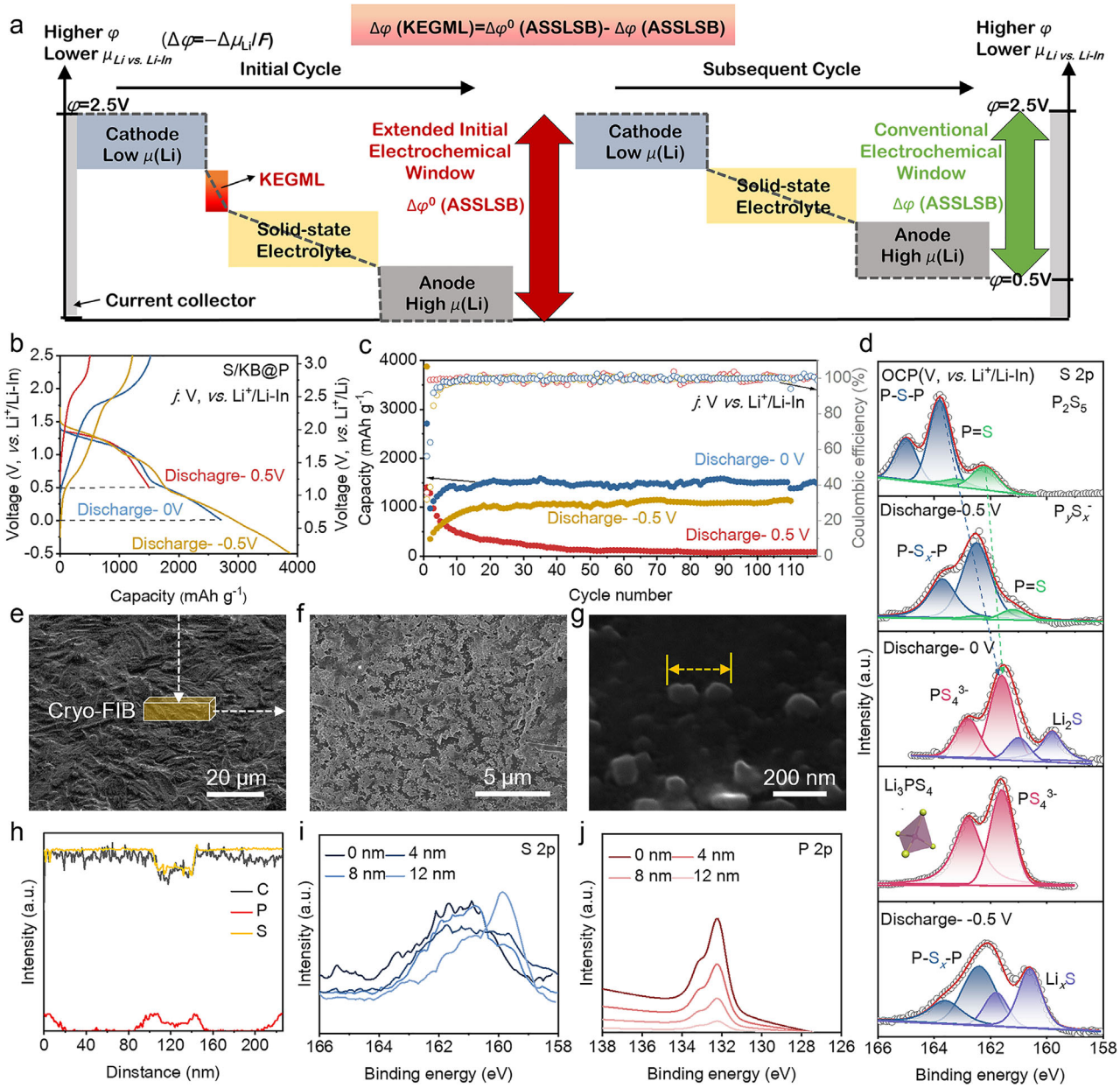

Figure 2. a) Schematic diagram of the applied electrochemical window (color bars) for KEGML-based ASSLSB operation. The variables μ and φ are the chemical potential and the electric potential, respectively. The symbol F represents the electric force, which is used to explain the relationship between electric charge and potential difference. b) Discharge-charge profiles and c) cyclic performance of S/KB@P cathode with an active loading of 1 mg cm^{-2} at 0.1C under different discharge cut-off potentials, and d) S 2p XPS spectra of S/KB@P-LiI cathode at the corresponding discharge cut-off potential. e–g) Cryo-FIB-SEM images. h) P, S, and C SEM-EDX line scans in the line visualized in 2g. i) S 2p, and j) P 2p in-depth profile XPS spectra of the S/KB@P-LiI cathode discharged to 0 V versus Li$^+$/Li-In.

conducted to investigate the compositional evolution of the S/KB@P cathode during (dis)charging. As shown in the CV curves (Figure S13a, Supporting Information), cathodes both exhibit one pair of broad reduction and oxidation peaks ≈1.0 and 2.0 V versus Li$^+$/Li-In associated with the solid-state conversion of S. The main difference between them is that one broad peak after 0.5 V versus Li$^+$/Li-In in the initial cathodic sweep of the S/KB@P cathode, presumably attributed to the lithiation reaction of the P_2S_5 compounds formed on S/KB@P. The CV curve of the S/KB@P cathode during the initial cycle with a lower cut-off potential is applied (Figure S13b, Supporting Information). The broad peak is observed within the voltage range of 0.5 to −0.5 V versus Li$^+$/Li-In. This conversion reaction and the corresponding products can be identified by ex situ XPS analyses shown in Figure 2d. Figure S14 (Supporting Information) suggests that LiI is not the primary redox center.[34] The S 2p (Figure 2d) and P 2p (Figure S15a, Supporting Information) XPS spectra of the S/KB@P-LiI cathode at open circuit potential (OCP) (Table S3,

Supporting Information) exhibit chemical states that correspond to the P_2S_5 spectra. Upon discharge to 0.5 V versus Li^+/Li-In, the green peaks and the blue peaks gradually merge, with their intensity diminishing simultaneously, suggesting the initiated process of lithiation occurs in P_2S_5. Upon discharge to 0 V versus Li^+/Li-In, the two doublet peaks were merged and shifted to 162.8 and 161.6 eV, respectively. The peak locations and profiles become almost identical to those of the PS_4^- species in the commercial Li_3PS_4 powder. At the same time, the doublet peaks at 161.0 and 159.8 eV (purple-shaded areas) agree with the S 2p spectrum of the commercial Li_2S powder (Figure S12a, Supporting Information). After discharging to −0.5 V versus Li^+/Li-In, the locations of those peaks remarkably shift to higher binding energies, indicating the disappearance of Li_3PS_4. These results indicate that the potential-modulated process renders the cleavage of P═S and P—S—P bonds in P_2S_5 and generates Li_3PS_4 and Li_2S on the surface between the potential range of 0.5–0 V versus Li^+/Li-In. To further confirm this, a cathode with only P_2S_5 and LiI marked as KB-P_2S_5-LiI cathode was prepared and subjected to similar discharge conditions, followed by XPS measurements shown in Figure S16 and Table S4 (Supporting Information).[49,50] The XPS analysis results further indicate that the various chemical states of the potential-modulated KEGML are consistent with the chemical states of KEGML during its growth process on the S/KB@P cathode.

Subsequently, a cryo-FIB-SEM was employed to maintain the chemical integrity of the S/KB@P-LiI cathode discharged to 0 V versus Li^+/Li-In (Figure 2e).[51,52] Figure 2f illustrates a cross-section of the composite particles in solid-solid contact within the plane of the cut cathode. A line on the cross-section obtained through cryo-FIB treatment of individual composite particles (Figure 2g) was analyzed using EDX. The P component at the surface of the single composite exhibits a gradual variation along its edges and a progressive decline in phosphate-based concentration from its outer surface toward its interior (Figure 2h). An in-depth XPS profile exhibits a significant decrease in the intensity of S 2p peaks associated with PS_4^{3-} while an increase is observed in peaks related to Li_2S as the etching depth increases (Figure 2i). A remarkable decrease in P 2p peaks associated with PS_4^{3-} upon etching (Figure 2j). In addition, a gradient modulator exhibits a smooth transition in P and S composition (Figure S17a,b, Supporting Information). These findings confirm the radial gradient. Moreover, the expected persistence of the gradient is further confirmed through in-depth XPS spectra after extended cycling (Figure S15b,c, Supporting Information). This long-term stability of the gradient may be a key factor contributing to the high performance. Figure S17c,d (Supporting Information) confirms the presence of KEGML at the contact interface within a group of particles. The potential-modulated KEGML ensures a homogenous distribution throughout the cathode material, facilitating easy access for Li^+ activation and interaction within the interfacial-internal S.

2.2. Electrochemical Performance of KEGML-Based ASSLSBs

The introduction of a higher amount of P (up to 10%) in the pre-reaction process results in an increased overpotential on its charge/discharge voltage profiles (**Figure 3a**). The XPS P 2p spectra of the S/KB@P(10%) cathode in Figure S18a (Supporting Information) exhibit not only peaks corresponding to P_2S_5 but also peaks indicative of P. It demonstrates that the amount of added P is excessive; the presence of unreacted P with ion and electron insulation will result in an increase in ionic/electronic resistance (Figure S18b,c, Supporting Information), leading to a rise in overpotential. While the S/KB cathode without P does not show a large overpotential (Figure 3a), it suffers from a low capacity and rapid capacity fading (Figure 3b,c). Although the rate capability of the S/KB@P(10%) cathode is slightly better than that of the S/KB cathode, but significantly lower than that of the S/KB@P cathode. The S/KB@P(10%) cathode demonstrates a low capacity of 895.1 mAh g^{-1} but excellent capacity retention (Figure 3c). Based on the comprehensive evaluation of the electrochemical properties presented above, the optimum P content in the S/KB@P cathode was determined to be 4%. The S/KB@P cathode exhibits outstanding ultra-long cycling stability (≈1.5 years), retaining 99.9% of its capacity and maintaining a high reversible capacity of 1579 mAh g^{-1} as high as 558.3 mAh g^{-1} based on the total cathode weight. The XPS measurement was conducted to further investigate the failure reason of the S/KB cathode. It is found that the peak location associated with LPSC changes during cycling, and there is incomplete conversion of S (Figure S19a,b and Table S5, Supporting Information). In comparison, there are no characteristic peaks related to incomplete conversion of Li_2S or decomposition of LPSC in the S 2p spectra of the S/KB@P cathode, indicating that the KEGML promotes reaction kinetics for full-sulfur conversion and improves stability.

To further reveal the enhanced reaction kinetics, a CV test at different scan rates from 0.1 to 1.0 mV s^{-1} was conducted to determine the Li-ion diffusion coefficient. As shown in Figure S20 (Supporting Information), the S/KB@P cathode exhibits a higher current intensity and lower overpotential than the S/KB cathode, which indicates that KEGML can enhance Li^+ transport and reaction kinetics. In addition, the cathodic slope and anodic slope of S/KB@P are 1.91 and 1.74, respectively, which are higher than the S/KB 0.62 reduction peak and 0.49 oxidation peak, indicating the Li_3PS_4-based KEGML can promote the Li^+ transport for redox from the estimated Li^+ diffusion coefficient. Two important conclusions can be reached from the results above: 1) The formation of the Li_3PS_4-KEGML facilitates ion transport within the composite electrode particles, enhancing S utilization and promoting fast reaction kinetics in the cathode. 2) The Li_3PS_4-KEGML improves stability while reducing the decomposition of LPSC. As a result, the S/KB@P cathode demonstrates the highest specific capacity (based on the total cathode weight) at room temperature, while also exhibiting exceptional cycle life (Figure 3d).[14,18,20,33,53–58]

After 1000 cycles at 2C, a specific capacity of 454.3 mAh g^{-1} is maintained, implying a capacity retention rate of 69% (Figure S21, Supporting Information). Even under high loading conditions, the presence of the Li_3PS_4-KEGML maintains it at 1524 mAh g^{-1} after 210 cycles with a loading of 8.4 mg cm^{-2} (Figure S22a, Supporting Information; Figure 3e). The achieved maximum areal capacity is 13.0 mAh cm^{-2}. With a maximum loading of 10.2 mg cm^{-2}, the discharge areal capacity reaches 7.1 mAh cm^{-2} (Figure S22b,c, Supporting Information). It exhibits the highest areal capacity among all reported cathodes after more

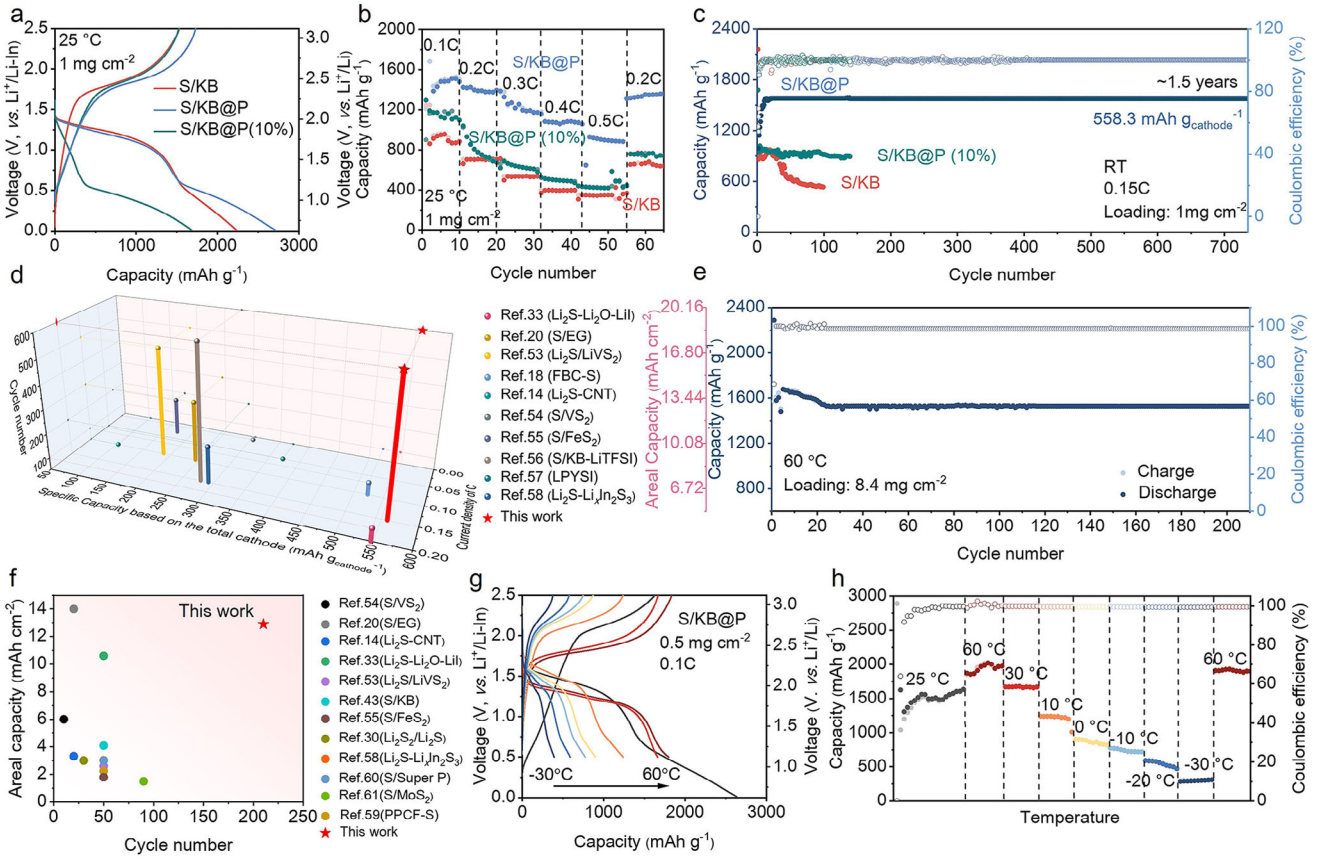

Figure 3. a) Initial discharge-charge voltage profiles at 0.1C, b) Rate capability, and c) cycling performance of S/KB, S/KB@P, and S/KB@P(10%) cathodes. d) Cycling performance and capacity comparison. e) Cycling performance at 0.1C with active loading of 8.4 mg cm^{-2}. f) Cycling performance and areal capacity comparison. g,h) Electrochemical performance at 0.1C of Li_3PS_4-KEGML-based ASSLSBs at different temperatures.

than 200 cycles (Figure 3f).[14,20,30,33,43,53–55,58–61] The rate capability of the S/KB@P cathode at varying temperatures indicates a discharge capacity of 310 mA h g^{-1} with CE of 99.4% at −30 °C, respectively (Figure 3g,h). When the temperature returns to 60 °C, the rechargeable discharge capacity reverts to 1902 mA h g^{-1} with a CE of 99.4%, indicating substantial resistance to temperature fluctuations. Furthermore, the retaining capacity of KEGML-based ASSLSBs for up to 100 cycles at both −30 and 60 °C indicates outstanding cycle stability (Figure S23a,b, Supporting Information). At the same time, the gradual decrease in the P concentration with increasing etching depth suggests that the gradient of the KEGML remains stable at both −30 and 60 °C (Figure S23c,d, Supporting Information). These findings indicate the structural and long-term stability of KEGML-enabled ASSLSBs under wide-temperature conditions.

2.3. Coupling Reaction Mechanism on KEGML-Based ASSLSBs

In situ Raman was conducted to investigate the coupling electrochemical reaction mechanism of the KEGML-based ASSLSBs (**Figure 4a**; Figure S24, Supporting Information). The Raman spectra are presented for a detailed analysis of the KEGML forming process (Figure 4b; Figure S25, Supporting Information). Figure S26a (Supporting Information) shows the Raman spectra of commercial S and Li_3PS_4 as references. Initially, the S/KB@P composite exhibits broad peaks at 471, 245, and 217 cm^{-1} attributed to the S—S bond in S, along with peaks at 390 cm^{-1} associated with the P-S-P bond.[45,46] Meanwhile, stretching vibrations of the P═S bond are observed at ≈686 and 712 cm^{-1}.[45,46,62] The Raman fingerprints of P_2S_5 are observed at 390, 686, and 712 cm^{-1}, with corresponding to the T2 and A1 modes.[62] These peak positions in wavenumbers are consistent with the commercial P_2S_5 Raman singles in Figure S26b (Supporting Information). During the initial discharge process, the P═S bond disappears and the P—S—P bond splits into P—S bonds at 370 and 410 cm^{-1}.[45,46,49] The peak at 410 cm^{-1} gradually shifts upward to 420 cm^{-1} at 0 V versus Li^+/Li-In, accompanied by the appearance of a new peak at 290 cm^{-1}, denoting the formation of Li_3PS_4-KEGML.[49] This result is consistent with that of the XPS spectra in Figure 2d. During the formation of KEGML, the peak associated with Li_2S_x is observed at 451 cm^{-1},[63] which vanishes as the discharge ends. Simultaneously, the peaks linked to the Li-S bond from Li_2S are visible at 375 cm^{-1} consistent with the peak position wavenumbers of Li_2S singles in Figure S26b (Supporting Information),[64] suggesting the transformation of intermediate phases Li_2S_x followed by its conversion into Li_2S, alongside the conversion of S/Li_2S. It is noteworthy that Li_3PS_4-KEGML remains visible in the subsequent cycles under a potential window of 0.5–2.5 V versus Li^+/Li-In, while reversible conversion

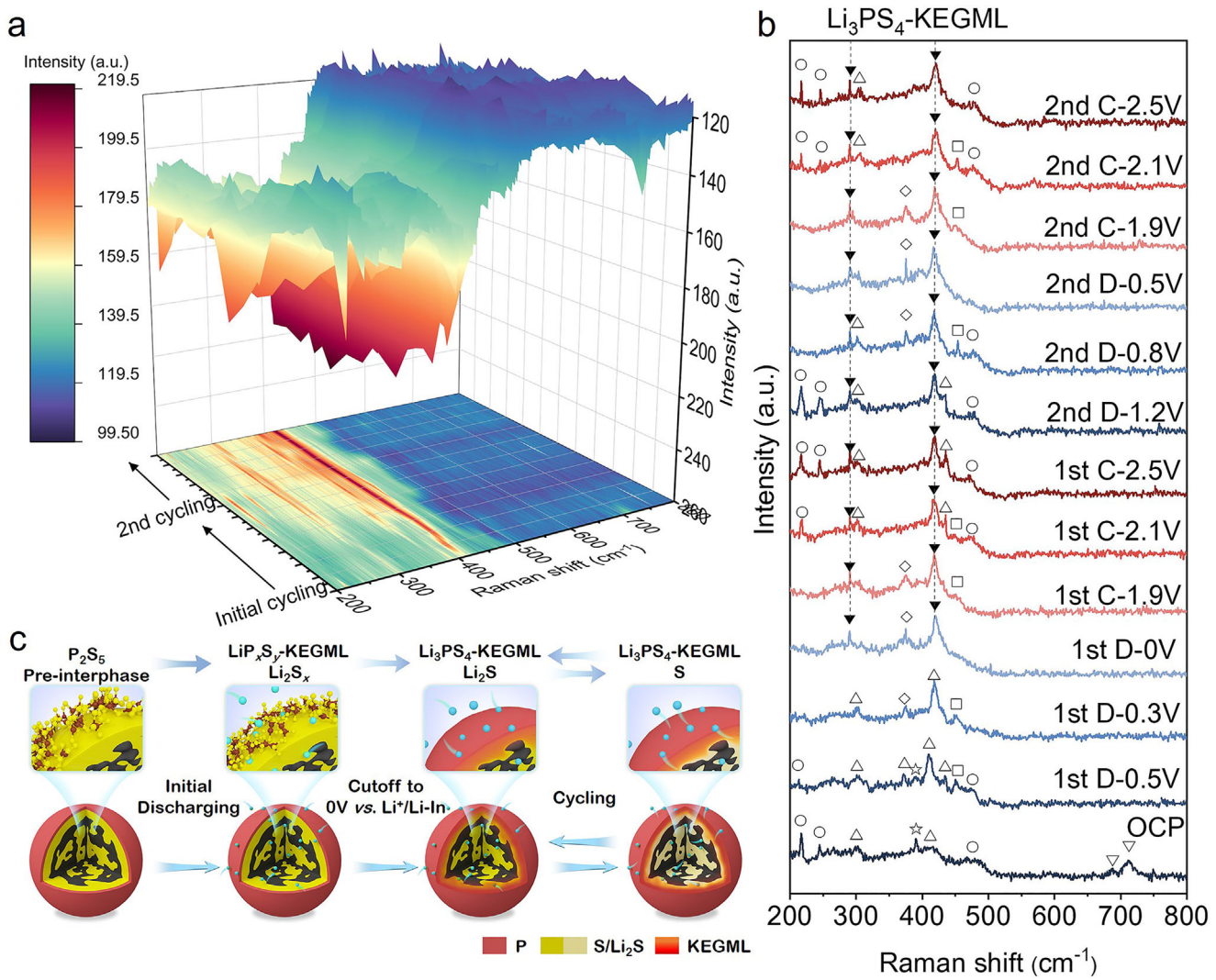

Figure 4. In situ Raman spectra to unravel the electrochemical cycling mechanism. a) 3D contour plots and b) corresponding spectra analysis (▼peaks from the Li_3PS_4, ☆peaks from the P-S-P, ▽peaks from the P═S, △peaks from the P—S, °peaks from the S—S,◇peaks from the Li_2S, and □peaks from the Li_2S_x). c) Schematic of the coupling reaction mechanism.

reactions between S and Li_2S take place. The electrochemical cycling mechanism is summarized in Figure 4c. Through an extension of the initial discharge cut-off potential, the P_2S_5 pre-interphase at S/KB undergoes a reaction with Li-ion, resulting in the formation of KEGML. In detail, the pre-interphase of P_2S_5 transforms with Li ion into a Li_3PS_4-KEGML across the radius of the composite particle's surface at the discharge potential of 0 V versus Li^+/Li-In. The initial electrochemical window of the ASSLSB is extended by the electrochemical window provided by the KEGML (Figure 2a). Then, a narrower conventional electrochemical window (0.5–2.5 V vs Li^+/Li-In) is adopted in the subsequent cycle to ensure the existence of KEGML. It is similar to the pre-lithiation process, a portion of Li-ions is stored through reaction with the P_2S_5 pre-interface during the initial discharge cycle. Therefore, the Li_3PS_4-KEGML exhibits stability, facilitating ionic transport within the S/KB cathode particles during extended cycling under 0.5–2.5 V versus Li^+/Li-In.

2.4. Interface Charge Transport Evolution of KEGML-Based ASSLSBs

Based on the Nyquist plots of the Li-In/LPSC/Li-In symmetrical cell and considering the equivalent circuit, the resistance values of LPSC (R_{SSE}) and LPSC/Li-In interface ($R_{1SSE/LiIn}$) are determined (Figure S27a, Supporting Information).[38,65,66] During cycling, the ASSLSBs were dismantled and reassembled with the corresponding voltage state (Figure S27b, Supporting Information). At the initial state, the total resistance of a Li-In/LPSC/cathode/LPSC/Li-In symmetrical cell (R_{total}) can be described according to Equation (1):[38,65,66]

$$R_{total} = R_t + 2R_{SSE} + 2R_{1SSE/LiIn} \quad (1)$$

where R_t represents the effective ionic transport resistance within the cathode composite.[38,65,66] However, the R_{SSE} and $R_{1SSE/LiIn}$ differ from the state after (dis)charging due to interfacial side

reactions and redox of LPSC (highlighted red interface in Figure S27b, Supporting Information).[12,38,40] Therefore, the R_{total} of Li-In/LPSC/cathode/LPSC/Li-In symmetrical cells can be reasonably described by Equation (2):

$$R_{total} = R_{SSE} + R_{1SSE/LiIn} + R_t + R_s + R_{2SSE/LiIn} \quad (2)$$

where R_S and $R_{2SSE/LiIn}$ represent the resistance of LPSC and the interface resistance between LPSC and Li-In after cycling, respectively. Therefore, the R_t, R_S, and $R_{2SSE/LiIn}$ are variables that need to be fitted according to the impedance spectrum (as indicated in the red box in Figure S27b, Supporting Information). The impedance parameter values according to the equivalent circuit (Figure S27c, Supporting Information inset) are listed in Tables S6 and S7 (Supporting Information). The error values associated with impedance fitting, exported by "Zview" software, are also incorporated into Tables S6 and S7 (Supporting Information). The Nyquist plots and corresponding fitting results are collected at different potentials during the 20th and 200th cycles (Figure S27c–h, Supporting Information).

During the initial cycle, there is no significant alteration in the R_t of the S/KB@P cathode even after the 200th cycle (**Figure 5a**). Comparatively, the R_t and R_s of the S/KB cathode sharply increased during the initial discharging process and did not revert to their initial level until the initial charge process, but exhibited a significant increase after 200 cycles. The rapid increase of the S/KB cathode can be attributed to the reversible decomposition of LPSC. This reversible decomposition is not conducive to long-term cycling stability, as evidenced by the increased impedance value after 200 cycles.[12,38,39,67,68] The impedance of the S/KB@P cathode is generally found to be lower and more stable compared to that of the S/KB cathode. Ionic transference numbers of symmetrical cells for the S/KB@P cathode are more stabilized and higher than those of the S/KB cathode (Figures S28–S30 and Table S8, Supporting Information). These results indicate that the initial-potential-modulated KEGML contributes to interfacial stability and reduces ion transport impedance. Additionally, the Li_3PS_4-KEGML is more effective in addressing inadequate Li^+ transportation caused by solid-solid interfacial contact and improving conversion reaction kinetics than other chemical-state KEGML.

The ionic transport capability (σ_i) during cycling was evaluated and calculated by Equation (3):

$$\sigma_i = \frac{L}{(R_t + R_s)A} \quad (3)$$

where L represents the thickness of the cathode&LPSC layers (0.099 cm), and A denotes the electrode area (0.785 cm^2) (Table S9, Supporting Information). Before initial discharging to 0.5 V versus Li^+/Li-In, there is no significant difference in σ_i between the S/KB@P and S/KB cathodes (Figure 5b). During the process from initial discharge at 0.5–0 V versus Li^+/Li-In, the σ_i of the S/KB@P cathode undergoes a decrease followed by an increase, but there is a sharp decrease in the S/KB cathode. This indicates that KEGML stabilizes the conductivity of the cathode during the initial potential modulation. The σ_i of the S/KB@P cathode consistently exceeds that of S/KB during the subsequent cycle. The difference in σ_i between S/KB@P and S/KB cathodes becomes more pronounced at the 200th cycle. The Li_3PS_4-KEGML irreversibly formed at 0 V versus Li^+/Li-In, facilitates stable Li^+ transport during subsequent cycles with a potential window of 0.5–2.5 V versus Li^+/Li-In, thereby creating the necessary conditions for a high-performance sulfur cathode. Compared to the S/KB cathode without KEGML, there is a nearly eightfold increase in ionic transport capability achieved by the S/KB cathode with KEGML at the end of the 200-cycle. The ionic conductivity values obtained from the direct-current (DC) polarization method are further provided for quantified and comparison (Figures S31–S36 and Table S10, Supporting Information). The variation trend of ionic conductivity aligns with that obtained through the above AC impedance measurements. It has been further verified that a nearly eightfold increase in ionic transport capability by KEGML.

To investigate the interfacial evolution of the cathode during cycling, galvanostatic intermittent titration technique (GITT) and electrochemical impedance spectroscopy (EIS) were employed (Figures S37,S38, Supporting Information). The apparent smaller charge transfer resistance and energetic reaction kinetics within the cathode after the initial (dis)charging can be attributed to the KEGML and S activation.[69,70] Some specific electrochemical processes exhibit closely matched time constants, which can cause the semicircular regions of their EIS spectra to become coupled. This coupling makes it difficult to fit equivalent circuits, especially in all-solid-state battery systems.[71–73] Thus, the impedance spectra were further analyzed using the DRT method (Figure 5c), which enables a direct differentiation of electrochemical processes by utilizing the sensitivity of diverse electrochemical reactions over time.[71,74] This simplifies the analysis of impedance spectra and significantly enhances their kinetic resolution accuracy over different time scales.[74,75]

The detailed DRT curves corresponding to the contour plots are shown in Figure S39 (Supporting Information). The peak at 10^{-6} s corresponds to the impedance of the grain boundary within the SSEs.[76,77] This impedance is relatively small compared to the overall ASSLSBs' impedance contribution at other relaxation times.[71] The peaks between 10^{-1}–100 s and 100–10^1 s correspond to the interfacial transport impedance of the Li-In/LPSC and the cathode/LPSC, respectively.[71] The peak situated at 10^2 s corresponds to the charge transfer impedance within the cathode.[70,78] The magnitudes of these impedances are represented by the areas and intensities of their corresponding peaks. Throughout the cycling, the impedance of the S/KB@P cathode is consistently lower than that of the S/KB cathode, indicating superior reaction kinetics. Particularly at the 200th cycle, a noticeable difference in charge transfer impedance suggests that fast reaction kinetics and effective ion transport are maintained within the S/KB@P cathode during the long cycle due to the presence of the Li_3PS_4-KEGML.

2.5. Computational Simulation of KEGML Assisting Interface Stability and Ion Transport

The evolution of the nanoscale contact interface within the S/KB@P cathode during (dis)charging was further explored using AIMD simulations (**Figure 6a**). After discharging for 300 ps, there are no decomposition or recombination reactions

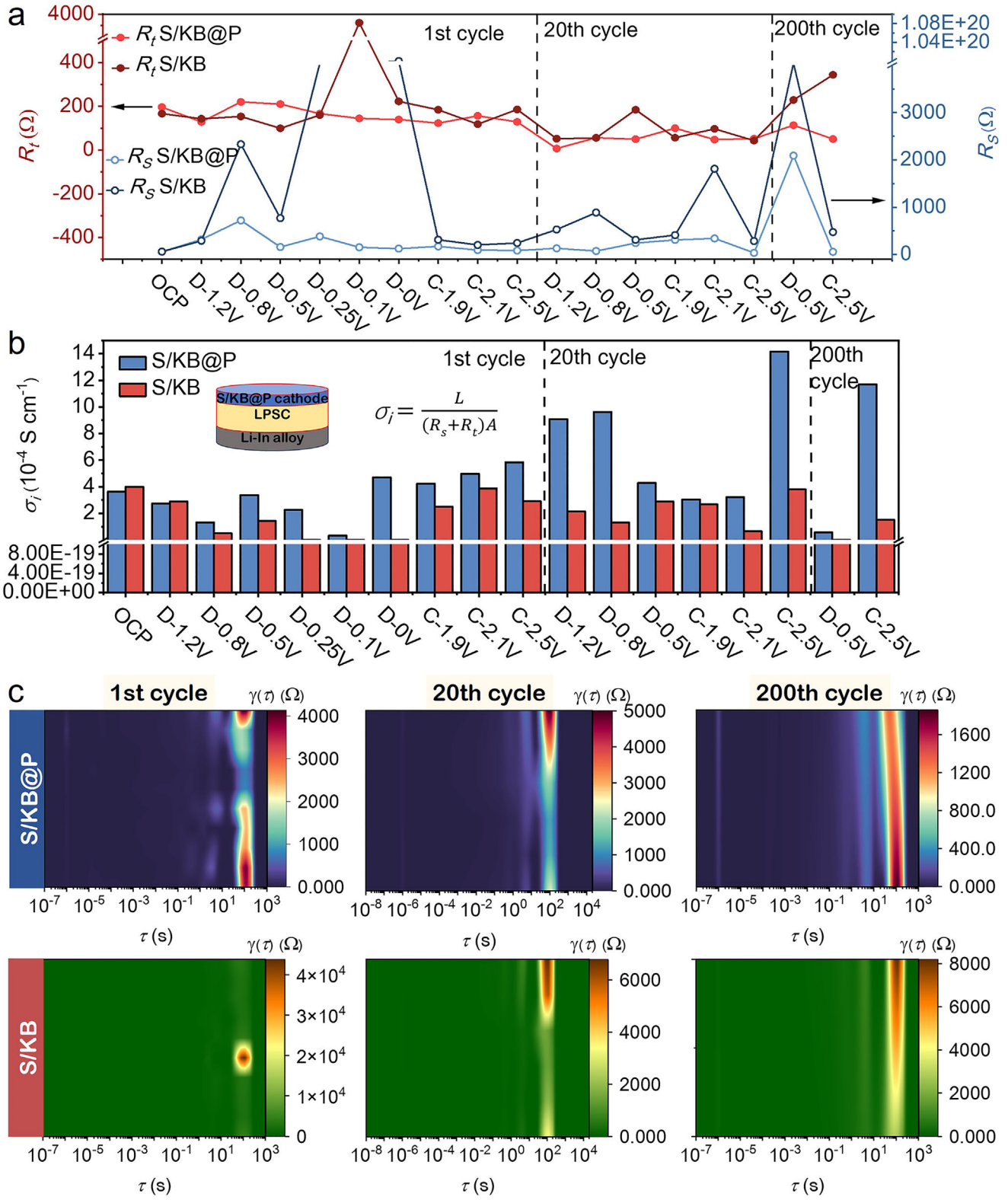

Figure 5. a) Impedance parameter values according to the equivalent circuit. b) Calculated ion conductivities (cathode & LPSC layers). c) DRT analysis of S/KB@P cathode and S/KB cathode at the 1st, 20th, and 200th cycle.

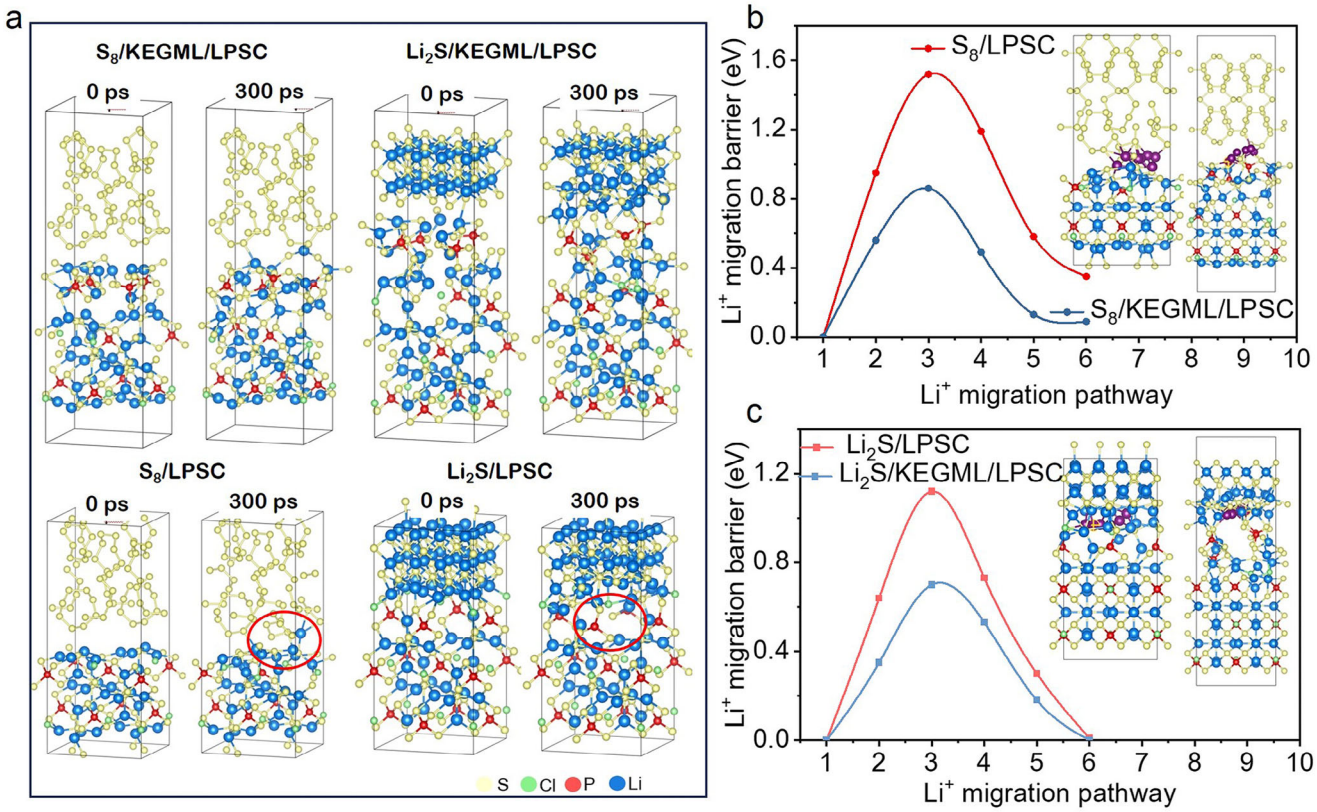

Figure 6. a) Structural changes of the selected S_8/KEGML/LPSC, Li_2S/KEGML/LPSC, S_8/LPSC, and Li_2S/LPSC models after AIMD simulations (300 ps). b) Energy profiles along the Li^+ migration pathways at b) S_8/KEGML/LPSC, S_8/LPSC, c) Li_2S/KEGML/LPSC, and Li_2S/LPSC interfaces.

observed across the interfaces of S_8/KEGML/LPSC. However, the interfaces of S_8/LPSC without the interphase of Li_3PS_4 exhibit a disordered appearance, which is highlighted with the red circle. During charging to 300 ps, the composition of the material located at the interface between Li_2S/KEGML/LPSC remains relatively stable. Comparatively, structural changes are observed at the Li_2S/LPSC interface, where broken LPSC leads to the presence of trigonal pyramidal PS_3 as indicated by the red circle. The depletion of LPSC caused by Li_2S damages the ionic transport pathway around the active material, and this damage accumulates during ASSLSB cycling, affecting long-term electrochemical reactions.[12,13]

The averaged interface energies calculated can be utilized to further estimate the stability of the interface (Figure S40, Supporting Information). The higher the average excess of interfacial energy, the more stable the reaction interface becomes, reducing the likelihood of interfacial diffusion and preventing material loss and changes in the chemical state at the interface.[12,13,79,80] The migration energy barrier of Li^+ at the interface implies that Li_3PS_4-KEGML exhibits a reduced energy barrier for Li^+ migration, thereby indicating its favorable impact on ion transport (Figure 6b,c). The migration path is illustrated by purple spheres. Overall, the Li_3PS_4-KEGML not only functions as an efficient ionic pathway but also enhances the stability of the internal contact interfaces within the cathode during cycling and prevents LPSC depletion and interfacial diffusion phenomena. These effects demonstrate the benefits of Li_3PS_4-KEGML in improving interfacial stability for enhanced electrochemical performance during cycling.

3. Conclusion

Herein, a highly ionic-conductive and interface-stabilized KEGML was in situ constructed via potential modulation within ASSLSBs. The main functions of KEGML to boost the electrochemical performance of ASSLSBs can be concluded as follows: 1) Activates the S and improves the S utilization; 2) Improves ion transport in a nearly eightfold factor and accelerates reaction kinetics; 3) Alleviates the problems of interfacial side reactions, ion pathway failure resulting from LPSC decomposition, and possible depletion of S or Li_2S/LPSC during long-term cycling and improves interfacial stability. Among all chemical states of KEGML, the Li_3PS_4-KEGML-based ASSLSBs demonstrate outstanding electrochemical behavior, with an exceptional cycling stability of 99.9% capacity retention for ≈1.5 years with a specific capacity of 1578.9 mAh g^{-1}. Employing high S-loading electrodes, the cathode reaches a high areal capacity of 13 mAh cm^{-2}. Furthermore, the cathode displays remarkable adaptability to temperature variations. This work presents a novel route to simultaneously achieve the complete solid-state conversion of S and ultra-long cycle stability by modulating the potential, providing valuable insights for the applied potential range of high-performance ASSLSBs.

Supporting Information

Supporting Information is available from the Wiley Online Library or from the author.

Acknowledgements

H.L. and L.C. contributed equally to this work. The authors thank the Center of Cryo-Electron Microscopy at Zhejiang University for granting us access to their Cryo-FIB-SEM characterization equipment. The authors are grateful to the financial support from the National Natural Science Foundation of China (T2241003), the National Key Research and Development Program of China (2022YFB4003500), and the Key R&D project of Hubei Province, China (2021AAA006). A.C. acknowledges support from the 2BoSS project of the ERA-MIN3 program with the Spanish grant number PCI2022-132985/AEI/10.13039/ 501100011033 and Generalitat de Catalunya 2021SGR01581.

Conflict of Interest

The authors declare no conflict of interest.

Data Availability Statement

The data that support the findings of this study are available in the supplementary material of this article.

Keywords

all-solid-state lithium-sulfur battery, electrode/electrolyte interface, solid electrolyte, ultralong life, wide-temperature range

Received: March 5, 2025
Revised: May 19, 2025
Published online:

[1] F. Wu, S. Fang, M. Kuenzel, A. Mullaliu, J. K. Kim, X. Gao, T. Diemant, G. T. Kim, S. Passerini, *Joule.* **2021**, *5*, 2177.
[2] J. E. T. Bistline, *Joule* **2021**, *5*, 2551.
[3] S. Fang, F. Wu, S. Zhao, M. Zarrabeitia, G. T. Kim, J. K. Kim, N. Zhou, S. Passerini, *Adv. Energy Mater.* **2023**, *13*, 2302577.
[4] G. Zhou, H. Chen, Y. Cui, *Nat. Energy* **2022**, *7*, 312.
[5] Q. Pang, X. Liang, C. Y. Kwok, L. F. Nazar, *Nat. Energy* **2016**, *1*, 16132.
[6] J. T. Kim, X. Hao, C. Wang, X. Sun, *Matter* **2023**, *6*, 316.
[7] B. B. Gicha, L. T. Tufa, N. Nwaji, X. Hu, J. Lee, *Nano-Micro Lett.* **2024**, *16*, 172.
[8] F. Wu, Z. Chen, S. Fang, W. Zuo, G. T. Kim, S. Passerini, *Energy Storage Mater.* **2023**, *63*, 103062.
[9] Y. Kato, S. Hori, T. Saito, K. Suzuki, M. Hirayama, A. Mitsui, M. Yonemura, H. Iba, R. Kanno, *Nat. Energy* **2016**, *1*, 16030.
[10] S. Ohno, W. G. Zeier, *Acc. Mater. Res.* **2021**, *2*, 869.
[11] J. Janek, W. G. Zeier, *Nat. Energy* **2023**, *8*, 230.
[12] L. E. Camacho-Forero, P. B. Balbuena, *Chem. Mater.* **2019**, *32*, 360.
[13] H. Zhong, Y. Su, R. Ma, Y. Luo, H. Lin, J. Gu, Z. Gong, Y. Yang, *Adv. Funct. Mater.* **2024**, *34*, 2315925.
[14] M. Jiang, G. Liu, Q. Zhang, D. Zhou, X. Yao, *ACS Appl. Mater. Interfaces* **2021**, *13*, 18666.
[15] M. Yamamoto, S. Goto, R. Tang, K. Nomura, Y. Hayasaka, Y. Yoshioka, M. Ito, M. Morooka, H. Nishihara, T. Kyotani, *ACS Appl. Mater. Interfaces* **2021**, *13*, 38613.
[16] B. Chen, S. Deng, M. Jiang, M. Wu, J. Wu, X. Yao, *Chem. Eng. J.* **2022**, *448*, 137712.
[17] C. Wei, C. Yu, L. Peng, Z. Zhang, R. Xu, Z. Wu, C. Liao, W. Zhang, L. Zhang, S. Cheng, J. Xie, *Mater. Adv.* **2022**, *3*, 1047.
[18] S. Jin, M. Wang, Y. Zhong, X. Wang, C. Gu, X. Xia, J. Tu, *Mater. Today Sustain.* **2023**, *21*, 100281.
[19] H. Li, J. Song, F. Wu, R. Wang, D. Liu, H. Tang, *Nano Res.* **2023**, *16*, 10956.
[20] G. Xu, Z. Yan, H. Yang, X. Zhang, Y. Su, Z. Huang, L. Zhang, Y. Tang, Z. Wang, L. Zhu, J. Lin, L. Yang, J. Huang, *Small* **2023**, *19*, 2300420.
[21] H. Jiang, Y. Han, H. Wang, Y. Zhu, Q. Guo, H. Jiang, W. Sun, C. Zheng, K. Xie, *J. Alloys Compd.* **2021**, *874*, 159763.
[22] Q. Zhang, N. Huang, Z. Huang, L. Cai, J. Wu, X. Yao, *J. Energy Chem.* **2020**, *40*, 151.
[23] D. Wang, Y. Wu, X. Zheng, S. Tang, Z. Gong, Y. Yang, *J. Power Sources* **2020**, *479*, 228792.
[24] H. Jiang, Y. Han, H. Wang, Y. Zhu, Q. Guo, H. Jiang, C. Zheng, K. Xie, *Energy Technol.* **2020**, *8*, 2000023.
[25] G. Chang, Y. Oh, S. Kang, J. Park, H. Lim, *Electrochim. Acta* **2020**, *358*, 136884.
[26] R. Guo, K. Zhang, W. Zhao, Z. Hu, S. Li, Y. Zhong, R. Yang, X. Wang, J. Wang, C. Wu, Y. Bai, *Energy Mater. Adv.* **2023**, *4*, 0022.
[27] J. Gu, H. Zhong, Z. Chen, J. Shi, Z. Gong, Y. Yang, *Chem. Eng. J.* **2023**, *454*, 139923.
[28] H. Li, R. Wang, J. Song, D. Liu, H. Gao, Y. Chao, H. Tang, *Energy Environ. Mater.* **2024**, *7*, 12687.
[29] X. Gao, X. Zheng, Y. Tsao, P. Zhang, X. Xiao, Y. Ye, J. Li, Y. Yang, R. Xu, Z. Bao, Y. Cui, *J. Am. Chem. Soc.* **2021**, *143*, 18188.
[30] J. T. Kim, A. Rao, H. Nie, Y. Hu, W. Li, F. Zhao, S. Deng, X. Hao, J. Fu, J. Luo, H. Duan, C. Wang, C. V. Singh, X. Sun, *Nat. Commun.* **2023**, *14*, 6404.
[31] M. Li, H. Pan, T. Liu, X. Xiong, X. Yu, Y. Hu, H. Li, X. Huang, L. Suo, L. Chen, *ACS Energy Lett.* **2022**, *7*, 766.
[32] Y. Hu, Z. Sun, Z. Zhang, S. Liu, F. He, Y. Liu, Z. Zhuang, F. Liu, *Adv. Energy Mater.* **2022**, *13*, 2202756.
[33] Y. Fujita, A. Sakuda, Y. Hasegawa, M. Deguchi, K. Motohashi, D. Jiong, H. Tsukasaki, S. Mori, M. Tatsumisago, A. Hayashi, *Small* **2023**, *19*, 2302179.
[34] Y. Fujita, T. Hakari, A. Sakuda, M. Deguchi, Y. Kawasaki, H. Tsukasaki, S. Mori, M. Tatsumisago, A. Hayashi, *ACS Appl. Energy Mater.* **2022**, *5*, 9429.
[35] J. Jiang, Q. Fan, S. Chou, Z. Guo, K. Konstantinov, H. Liu, J. Wang, *Small* **2021**, *17*, 1903934.
[36] T. Hakari, A. Hayashi, M. Tatsumisago, *Adv. Sustain. Syst.* **2017**, *1*, 1700017.
[37] H. Wan, B. Zhang, S. Liu, J. Zhang, X. Yao, C. Wang, *Nano Lett.* **2021**, *21*, 8488.
[38] S. Ohno, C. Rosenbach, G. F. Dewald, J. Janek, W. G. Zeier, *Adv. Funct. Mater.* **2021**, *31*, 2010620.
[39] S. Ohno, R. Koerver, G. Dewald, C. Rosenbach, P. Titscher, D. Steckermeier, A. Kwade, J. Janek, W. G. Zeier, *Chem. Mater.* **2019**, *31*, 2930.
[40] D. H. S. Tan, E. A. Wu, H. Nguyen, Z. Chen, M. A. T. Marple, J.-M. Doux, X. Wang, H. Yang, A. Banerjee, Y. S. Meng, *ACS Energy Lett.* **2019**, *4*, 2418.
[41] X. Sun, Q. Li, D. Cao, Y. Wang, A. Anderson, H. Zhu, *Small* **2022**, *18*, 2105678.
[42] F. Han, J. Yue, X. Fan, T. Gao, C. Luo, Z. Ma, L. Suo, C. Wang, *Nano Lett.* **2016**, *16*, 4521.
[43] A. S. Alzahrani, M. Otaki, D. Wang, Y. Gao, T. S. Arthur, S. Liu, D. Wang, *ACS Energy Lett.* **2021**, *6*, 413.
[44] P. Zhu, C. Yan, J. Zhu, J. Zang, H. Jia, X. Dong, Z. Du, C. Zhang, N. Wu, M. Dirican, X. Zhang, Y. Li, *Energy Storage Mater.* **2019**, *17*, 220.

[45] X. Li, J. Liang, Y. Lu, Z. Hou, Q. Cheng, Y. Zhu, Y. Qian, *Angew. Chem., Int. Ed.* **2017**, *56*, 2937.
[46] N. Tanibata, H. Tsukasaki, M. Deguchi, S. Mori, A. Hayashi, M. Tatsumisago, *J. Mater. Chem. A* **2017**, *5*, 11224.
[47] H. Nagata, Y. Chikusa, *J. Power Sources* **2014**, *263*, 141.
[48] H. Nagata, Y. Chikusa, J. Akimoto, *J. Power Sources* **2020**, *453*, 227905.
[49] X. Li, J. Liang, Banis, J. Luo, C. Wang, W. Li, X. Li, Q. Sun, Y. Hu, Q. Xiao, T.-K. Sham, L. Zhang, S. Zhao, S. Lu, H. Huang, R. Li, X. Sun, *Energy Storage Mater.* **2020**, *28*, 325.
[50] J. Song, X. Peng, D. Liu, H. Li, M. Wu, K. Fang, X. Zhu, X. Xiang, H. Tang, *J. Energy Chem.* **2023**, *80*, 381.
[51] M. J. Zachman, Z. Tu, S. Choudhury, L. A. Archer, L. F. Kourkoutis, *Nature* **2018**, *560*, 345.
[52] J. Z. Lee, T. A. Wynn, M. A. Schroeder, J. Alvarado, X. Wang, K. Xu, Y. S. Meng, *ACS Energy Lett.* **2019**, *4*, 489.
[53] C. Y. Kwok, S. Xu, I. Kochetkov, L. Zhou, L. F. Nazar, *Energy Environ. Sci.* **2023**, *16*, 610.
[54] S. Xu, C. Y. Kwok, L. Zhou, Z. Zhang, I. Kochetkov, L. F. Nazar, *Adv. Funct. Mater.* **2020**, *31*, 2004239.
[55] J. P. Mwizerwa, Q. Zhang, F. Han, H. Wan, L. Cai, C. Wang, X. Yao, *ACS Appl. Mater. Interfaces* **2020**, *12*, 18519.
[56] L. Hu, T. Yang, X. Yan, Y. Liu, W. Zhang, J. Zhang, Y. Xia, Y. Wang, Y. Gan, X. He, X. Xia, R. Fang, X. Tao, H. Huang, *ACS Nano* **2024**, *11*, 8463.
[57] B. Zhao, C. Zhou, P. Chen, X. Gao, *ACS Appl. Mater. Interfaces* **2024**, *16*, 4679.
[58] P. W. Yu, S. R. Sun, C. H. Sun, C. Y. Zeng, Z. Hua, N. Ahmad, R. W. Shao, W. Yang, *Adv. Funct. Mater.* **2024**, *34*, 2306939.
[59] X. Sun, Q. Li, D. Cao, Y. Wang, A. Anderson, H. Zhu, *Small* **2021**, *18*, 2105678.
[60] X. Zhu, W. Jiang, L. Wang, J. Lu, *Adv. Energy Mater.* **2024**, *14*, 2304244.
[61] H. Choi, H. Kim, M. J. Kim, Y. K. Sun, *ACS Appl. Mater. Interfaces* **2024**, *16*, 11076.
[62] X. Li, S. Guo, K. Jiang, Y. Qiao, M. Ishida, H. Zhou, *ACS Appl. Mater. Interfaces* **2018**, *10*, 16.
[63] N. Erika, T. S. Arthur, P. Bonnick, K. Suto, M. John, *MRS Adv.* **2019**, *4*, 2627.
[64] Z. Lin, Z. Liu, N. J. Dudney, C. Liang, *ACS Nano* **2013**, *7*, 2829.
[65] P. Minnmann, L. Quillman, S. Burkhardt, F. H. Richter, J. Janek, *J. Electrochem. Soc.* **2021**, *168*, 040537.
[66] N. Kaiser, S. Spannenberger, M. Schmitt, M. Cronau, Y. Kato, B. Roling, *J. Power Sources* **2018**, *396*, 175.
[67] B. Ding, J. Wang, Z. Fan, S. Chen, Q. Lin, X. Lu, H. Dou, A. Kumar Nanjundan, G. Yushin, X. Zhang, Y. Yamauchi, *Mater. Today* **2020**, *40*, 114.
[68] T. Swamy, X. Chen, Y.-M. Chiang, *Chem. Mater.* **2019**, *31*, 707.
[69] W. Ji, X. Zhang, D. Zheng, H. Huang, T. H. Lambert, D. Qu, *Adv. Funct. Mater.* **2022**, *32*, 2202919.
[70] X. Li, J. Liang, J. T. Kim, J. Fu, H. Duan, N. Chen, R. Li, S. Zhao, J. Wang, H. Huang, X. Sun, *Adv. Mater.* **2022**, *34*, 2200856.
[71] Y. Lu, C. Zhao, J. Huang, Q. Zhang, *Joule* **2022**, *6*, 1172.
[72] F. Ciucci, *Curr. Opin. Electroche.* **2019**, *13*, 132.
[73] J. Huang, Z. Li, B. Y. Liaw, J. Zhang, *J. Power Sources* **2016**, *309*, 82.
[74] B. A. Boukamp, *J Phys. Energy* **2020**, *2*, 042001.
[75] L. Chen, W. Song, N. Li, H. Jiao, X. Han, Y. Luo, M. Wang, H. Chen, S. Jiao, D. Fang, *Adv. Mater.* **2020**, *32*, 2001212.
[76] H. Li, R. Wang, S. Zhao, J. Song, Y. Liao, H. Tang, *Adv. Compos. Hybrid Mater.* **2023**, *6*, 162.
[77] J. Liu, F. Ciucci, *Electrochim. Acta* **2020**, *331*, 135316.
[78] X. Li, M. Ahmadi, L. Collins, S. V. Kalinin, *Electrochim. Acta* **2019**, *313*, 570.
[79] N. D. Lepley, N. A. W. Holzwarth, *Phys. Rev. B* **2015**, *92*, 214201.
[80] L. E. Camacho-Forero, P. B. Balbuena, *J. Power Sources* **2018**, *396*, 782.